AIAA JOURNAL
Vol. 37, No. 3, March 1999

Interaction of an Entropy Spot with a Shock

M. Y. Hussaini* and G. Erlebacher†
Florida State University, Tallahassee, Florida 32306-4120

The problem of a shock wave interacting with a two-dimensional and an axisymmetric entropy or temperature spot is addressed. The problem is posed in the framework of the Euler equations, which are solved by a sixth-order accurate shock-fitting algorithm. The results indicate that such an interaction squishes the spot in the direction of convection and engenders a pair of counter-rotating vortices along with an acoustic wave, which propagates away from the center of the vortical system. The acoustic front steepens, leading to secondary shocks for sufficiently high shock Mach numbers. The enstrophy and dilatation budgets are discussed. The quantitative differences between the hot and cold spot cases are brought out, as well as those between the two-dimensional and the axisymmetric cases. The emphasis is on the nonlinear aspects of the interaction process.

Nomenclature

A, B = matrices
C_1, C_2 = constants in Runge–Kutta scheme
c = speed of sound
d = dilatation
E_ω = percentage departure of maximum downstream vorticity from linear theory
h, k = grid spacing in X and Y
K = curvature tensor of the shock surface
M = Mach number
$\boldsymbol{n}$ = unit vector normal to the shock
$\mathcal{P}$ = $\log p$
p = pressure
$\boldsymbol{Q}$ = vector $(\mathcal{P}, u, v, s)$
R = grid stretching constant
$r_{\max}$ = maximum normal coordinate
r_0 = core radius of entropy spot
$r_{1/2}$ = half the nodes lie in $r < r_{1/2}$
s = entropy
T = temperature
t = time
$\boldsymbol{t}$ = unit vector tangent to the shock
U = mean streamwise velocity
$\mathcal{U}, \mathcal{V}$ = contravariant streamwise and normal velocity components
u, v = streamwise, normal velocity
$\boldsymbol{u}$ = velocity vector
X, Y = streamwise and normal computational coordinates
x, r = streamwise, normal (or radial) directions
α = 0 (two-dimensional flow), 1 (axisymmetric flow)
γ = ratio of specific heats
δ = $(\boldsymbol{u} - \boldsymbol{u}_s) \cdot \boldsymbol{n}$
ϵ = perturbation amplitude
ζ = ρc
ρ = density
τ = computational time
ω = vorticity
$\langle \cdots \rangle$ = average over downstream domain

Subscripts

i, j = grid point index
L = downstream boundary
m = mean value
s = shock
0 = dimensional reference value
1 = upstream

Superscript

b = buffer domain
i = Runge–Kutta stage
T = transpose
$*$ = scaled time
$'$ = perturbation variable
$\hat{}$ = unit vector

Received March 2, 1998; revision received Oct. 7, 1998; accepted for publication Oct. 18, 1998.

*Thinking Machine Corporation Chair in High Performance Computing and Director, Program in Computational Science and Engineering.
†Associate Professor of Mathematics, Program in Computational Science and Engineering.

Introduction

THE purpose of our continuing studies has been to unravel the various physical mechanisms underlying shock wave interaction processes.[1–11] To understand better such mechanisms, it is expedient to study them in isolation.[12–17] (An extensive list of references may be found in Ref. 3.) To this end, there have been studies of shock waves interacting with individual shear, sound, and entropy waves, which are interpreted as the Fourier components of arbitrary flows. If any one of these waves encounters a shock, it generates a triad of waves downstream of the shock. The linear theory relates the amplitudes of the waves downstream and upstream of the shock through the so-called transfer functions. Once the upstream flow is specified, in principle, it can be decomposed into Fourier components, and the downstream patterns can then be determined from the transfer functions associated with each Fourier component. In this fashion, Ribner[17] studied sound generated by the interaction of a single vortex with a shock. Although the interaction of a single entropy spot with a shock is clearly amenable to a similar approach, this problem does not appear to have been studied theoretically in this manner.

It is proper to mention here that the problem of entropy interaction with a shock, apart from its academic interest, has relevance to aerospace applications. For example, when a shock interacts with a turbulent boundary layer, an ubiquitous phenomenon in high-speed aerospace flows, the presence of entropy fluctuations is observed to enhance turbulence in such interactions. This problem has been a subject of computational and theoretical study by Mahesh et al.[12] In supersonic wakes, the density (and associated entropy) fluctuations are found to be relatively large, sometimes on the order of 40% of mean value, and the current study is particularly relevant to wake–shock interaction.[13] In hot rocket exhausts with oblique shock waves, entropy–shock interaction could be a predominant source of noise. Jackson et al.[5] have shown that, in the related case of reacting shocks, the noise generated by the interaction increases substantially with exothermicity. Another example is the combustor flowfield of a scramjet engine, where the mixing of the hot and cold jets of oxidant and fuel is enhanced through shock interaction.[18]

In the following sections, we present the physical problem, describe the numerical formulation and solution technique, discuss the

numerical results for two-dimensional and axisymmetric spots, and provide some conclusions.

Problem Statement and Solution Technique

Initially, a plane or axisymmetric shock front is established at $x = 0$ so that it moves in the positive x direction and interacts with a temperature spot in a quiescent fluid. We choose a frame of reference in which the initial shock is steady [Fig. 1, where the computational domain is bounded by $x = x_L(X = 0)$ on the left, by the shock $x = x_s(r, t)(X = 1)$ on the right, the symmetry axis $r = 0\,(Y = 0)$ at the bottom and the freestream range $r = r_{\max}$ at the top]. The flow upstream of the shock is defined by $\boldsymbol{u} = (U_1, 0)$, $T_1 = 1 + T_1'$, $P_1 = 1$, where

$$T_1' = \epsilon \exp\left\{-\tfrac{1}{2}\left[(x - x_c - U_1 t)^2 + r^2\right]\right\} \tag{1}$$

represents a simple mathematical model of a localized temperature disturbance. The flowfield between the shock front $x = x_s(r, t)$ and a certain left boundary $x = x_L < 0$ is assumed to be governed by the unsteady compressible Euler equations. In nondimensional variables, these equations are

$$\frac{\partial \mathcal{P}}{\partial t} = -\boldsymbol{u}\cdot\nabla\mathcal{P} - \gamma\nabla\cdot\boldsymbol{u}, \qquad \frac{\partial \boldsymbol{u}}{\partial t} = -\boldsymbol{u}\cdot\nabla\boldsymbol{u} - T\nabla\mathcal{P}$$
$$\frac{\partial s}{\partial t} = -\boldsymbol{u}\cdot\nabla s \tag{2}$$

where $\mathcal{P} = \log p$ is the logarithm of the pressure, $s = \log(p\rho^{-\gamma})$ is the entropy, ρ is the density, and T is the temperature. All variables are scaled with respect to their values in the initial undisturbed upstream state, denoted with a subscript 0. Thus, the pressure, density, and temperature are made nondimensional with respect to p_0, ρ_0, and T_0, respectively, whereas velocities are made nondimensional with respect to $(p_0/\rho_0)^{1/2}$, lengths with respect to the entropy spot core radius r_0, and time with respect to the ratio of length to velocity scale. The ratio of specific heat γ is assumed to be 1.4. Pressure, density, and temperature are, of course, related by the equation of state for an ideal gas $p = \rho T$.

The computational domain extends from $x = x_L$ on the left to the shock $x = x_s(y, t)$ on the right. In the vertical or the radial direction, it extends from $r = 0$ to $r_{\max}$. The transformation

$$X(x, r, t) = \frac{x - x_L}{x_s(r, t) - x_L}, \qquad Y(r) = \frac{r}{r_{\max}}\left(\frac{r_{\max}^2 + R^2}{r^2 + R^2}\right)^{\frac{1}{2}}$$
$$\tau = t \tag{3}$$

maps the computational domain onto the transformed space $0 \le X \le 1$, $0 \le Y \le 1$. The parameter R controls the grid clustering. If one-half of the grid points are to be located between $r = 0$ and $r_{1/2}$, then

$$R^2 = \frac{3r_{1/2}^2}{1 - 4r_{1/2}^2 r_{\max}^2} \tag{4}$$

subject to the constraint that $r_{1/2} < r_{\max}/4$. In the physical plane, the grid points move at the velocity $\boldsymbol{u}_g = X x_{s,t}\hat{\boldsymbol{x}}$. Thus, at the downstream boundary, the grid is fixed, whereas the grid points on the shock move with the shock velocity.

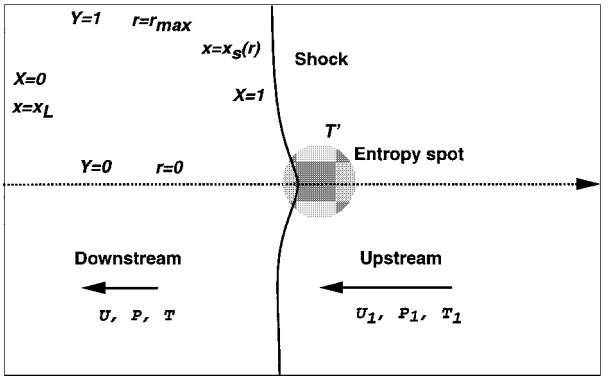

Fig. 1 Two-dimensional or axisymmetric geometry.

In the transformed plane, the Euler equations take the form

$$\frac{\partial Q}{\partial \tau} + A\frac{\partial Q}{\partial X} + B\frac{\partial Q}{\partial Y} = D \tag{5}$$

where

$$Q = (P, u, v, S)^T \tag{6}$$

$$A = \begin{bmatrix} \mathcal{U} & \gamma X_x & \gamma X_y & 0 \\ T & \mathcal{U} & 0 & 0 \\ 0 & 0 & \mathcal{U} & 0 \\ 0 & 0 & 0 & \mathcal{U} \end{bmatrix} \tag{7}$$

$$B = \begin{bmatrix} \mathcal{V} & \gamma Y_x & \gamma Y_y & 0 \\ 0 & \mathcal{V} & 0 & 0 \\ T & 0 & \mathcal{V} & 0 \\ 0 & 0 & 0 & \mathcal{V} \end{bmatrix} \tag{8}$$

and

$$D = (-\alpha\gamma(v/r), 0, 0, 0)^T \tag{9}$$

The contravariant velocity components are defined by

$$\mathcal{U} = \frac{\partial X}{\partial t} + u\frac{\partial X}{\partial x} + v\frac{\partial X}{\partial r} \tag{10}$$

$$\mathcal{V} = \frac{\partial Y}{\partial t} + u\frac{\partial Y}{\partial x} + v\frac{\partial Y}{\partial r} \tag{11}$$

The equation for the shock velocity is solved in the form given by Eq. (16). Two-dimensional and axisymmetric geometries are distinguished by the definition of the velocity divergence

$$\nabla\cdot\boldsymbol{u} = \frac{\partial u}{\partial x} + \frac{\partial v}{\partial r} + \alpha\frac{v}{r} \tag{12}$$

where $\alpha = 0$ for the two-dimensional flow and $\alpha = 1$ for the axisymmetric flow.

Boundary Conditions

The downstream outflow is subsonic for all shock strengths. The inflow at the shock boundary is supersonic, and all of the variables must be specified. These variables are obtained from the Rankine–Hugoniot conditions

$$p = [2/(\gamma + 1)]\left\{[(1 - \gamma)/2]p_1 + \rho_1\delta_1^2\right\} \tag{13}$$

$$\delta = (\gamma - 1)/(\gamma + 1)\delta_1 + [2\gamma/(\gamma + 1)](p_1/\rho_1\delta_1) \tag{14}$$

$$\boldsymbol{u}\cdot\boldsymbol{t} = \boldsymbol{u}_1\cdot\boldsymbol{t} \tag{15}$$

where $\delta_1 = \boldsymbol{u}_1\cdot\boldsymbol{n} - u_s\hat{\boldsymbol{x}}\cdot\boldsymbol{n}$ and $\delta = \boldsymbol{u}\cdot\boldsymbol{n} - u_s\hat{\boldsymbol{x}}\cdot\boldsymbol{n}$ ($u_s = \dot{x}_s$ is the perturbation velocity of the shock in the x direction). The unit vectors $\boldsymbol{n}$ and $\boldsymbol{t}$ are normal and tangential to the shock, respectively. The unknown shock velocity u_s is obtained from the evolution equation[10,19–21]

$$(u_s\hat{\boldsymbol{x}}\cdot\boldsymbol{n})_{,t} = \frac{(D - \zeta A)(\boldsymbol{n}\cdot\boldsymbol{u}_1)_{,t} + \zeta(\boldsymbol{u}\cdot\boldsymbol{n}_{,t})}{D + \zeta(1 - A)}$$
$$+ \frac{(E - \zeta B)p_{1,t} + (F - \zeta C)\rho_{1,t} - \mathcal{R}}{D + \zeta(1 - A)} \tag{16}$$

where $\zeta = \rho c$,

$$A = \frac{\gamma - 1}{\gamma + 1} - \frac{2\gamma}{\gamma + 1}\frac{p_1}{\rho_1\delta_1^2}, \qquad B = \frac{2\gamma}{\gamma + 1}\frac{1}{\rho_1\delta_1}$$
$$C = -B\frac{p_1}{\rho_1}, \qquad D = \frac{4\rho_1\delta_1}{\gamma + 1} \tag{17}$$
$$E = \frac{1 - \gamma}{\gamma + 1}, \qquad F = \frac{2\delta_1^2}{\gamma + 1}$$

$$\mathcal{R} = -\boldsymbol{u}\cdot\nabla p + \rho c\,\boldsymbol{n}\cdot(\boldsymbol{u}\cdot\nabla\boldsymbol{u}) - \gamma p\nabla\cdot\boldsymbol{u} + c\boldsymbol{n}\cdot\nabla p \qquad (18)$$

The downstream boundary $X=0$ is subsonic. We adopt the buffer domain technique developed by Ta'asan and Nark.[22] This technique modifies the equations governing the so-called buffer layer abutting the downstream boundary so that the outflow is supersonic. The modification involves replacing all time derivatives according to the prescription

$$\frac{\partial}{\partial t} \to \frac{\partial}{\partial t} + a(X)\frac{\partial}{\partial X} \qquad (19)$$

where $a(X)$ is an artificial velocity field, which is zero outside and varies smoothly inside the buffer zone. It is defined in such a way that the acoustic eigenvalues of the modified equations (expressed in transformed space)

$$U(0,Y,t) + a(0) \pm c\left[\left(\frac{\partial X}{\partial x}\right)^2 + \left(\frac{\partial X}{\partial r}\right)^2\right]^{\frac{1}{2}}$$

are all negative at the outflow boundary $X=0$. (The flow is from right to left.) The simple model function

$$a(X) = D\left[1 - (X/X_b)^2\right] \qquad (20)$$

produces little reflection on the downstream boundary if the width of the buffer zone is at least the characteristic length of the disturbance, which in this case is the width of the temperature spot. The constant D is defined as

$$D = 2.5\left\{c\left[\left(\frac{\partial X}{\partial x}\right)^2 + \left(\frac{\partial X}{\partial r}\right)^2\right]^{\frac{1}{2}} - U_1\right\} \qquad (21)$$

evaluated at $X=0$ when the simulation is initiated. The convective velocity $a(X)$ is such that the flow is subsonic as it enters the buffer zone and supersonic as it exits. Because the outflow is now supersonic, there is no longer any need for explicit boundary conditions. Details can be found in Ref. 10.

The freestream boundary $r = r_{\max}$ is sufficiently far away from the axis so that disturbances do not reach it during the course of the simulations. Thus, a zero perturbation condition can be appropriately imposed at this boundary.

Spatial Discretization

Spatial derivatives are all computed with a sixth-order compact method.[23] Consider just the X direction, the implementation in the Y direction being identical. Given a uniform grid $X_i = ih$, $i=0,\ldots,N$, derivatives of $u(X)$ with respect to X at points $i=2,\ldots,N-2$ satisfy

$$u'_{i-1} + 3u'_i + u'_{i+1} = \frac{u_{i+2} - u_{i-2} + 28(u_{i+1} - u_{i-1})}{12h} \qquad (22)$$

An explicit eighth-order stencil is used to compute derivatives for $i=0,1$:

$$u'_0 = \sum_{i=0}^{7} a_i u_i, \qquad u'_1 = \sum_{i=0}^{7} b_i u_i \qquad (23)$$

where $a^i = (-296/105, 415/48, -125/8, 985/48, -215/12, 791/80, -25/8, 145/336)$ and $b^i = (-3/16, -211/180, 109/48, -35/24, 115/144, -1/3, 23/240, -1/72)$. Derivatives u'_{N-1} and u'_N have similar expressions.

The streamwise velocity u and the thermodynamic variables are symmetric about $r=0$ in both two-dimensional and axisymmetric flows. On the other hand, the radial velocity v is antisymmetric. Derivatives at the axis and at the first point removed from the axis are computed by considering them as interior points and taking into account the symmetry properties of the dependent variables. If $u(r)$ is symmetric about $r=0$, derivatives of $u(Y)$ with respect to Y satisfy

$$u'_0 = 0 \qquad (24)$$

$$u'_1 = \frac{u'_3 - u'_1 + 28(u'_2 - u'_0)}{12k} \qquad (25)$$

whereas if $u(r)$ is antisymmetric about $r=0$,

$$u'_0 = \frac{u_2 + 28u_1}{6k} \qquad (26)$$

$$u'_1 = \frac{u'_3 + u'_1 + 28(u'_2 - u'_0)}{12k} \qquad (27)$$

where k is the uniform grid spacing in Y.

Time Advancement

The discretization of the spatial operators in Eq. (8) leads to a system of ordinary differential equations of the form

$$\frac{\mathrm{d}\boldsymbol{Q}_{ij}}{\mathrm{d}\tau} = \boldsymbol{L}_{ij} \qquad (28)$$

where $\boldsymbol{L}_{ij}$ is $-A\boldsymbol{Q}_X - B\boldsymbol{Q}_Y$ evaluated at the discrete point $X_i = ih$, $Y_j = jk$. An explicit low-storage fourth-order Runge–Kutta scheme is used to advance the solution from one time level to the next.[24] This scheme has five stages. Let $\boldsymbol{Q}^{n,0} = \boldsymbol{Q}^n$ be the solution vector at time t^n, where the second index in the superscript represents the current stage. This index ranges from 0 to 5, with $\boldsymbol{Q}^{n+1} = \boldsymbol{Q}^{n,5}$. Let $\boldsymbol{R}^i$ be a temporary vector used to accumulate data with $\boldsymbol{R}^0 = 0$. Although $\boldsymbol{Q}$ and $\boldsymbol{R}$ have an i index, only a single array is used in a practical implementation. The sequence of operations is

$$\begin{aligned} \boldsymbol{R}^i &= C_1^i \boldsymbol{R}^{i-1}, & \Delta t^i &= C_2^i \Delta t \\ \boldsymbol{R}^i &= \boldsymbol{R}^i + \boldsymbol{L}_{ij}(\boldsymbol{Q}^{n,i-1}), & \boldsymbol{Q}^{n,i} &= \boldsymbol{Q}^{n,i} + \Delta t^i \boldsymbol{R}^i \end{aligned} \qquad (29)$$

with $i=1,\ldots,5$; and

$$C_1^1 = 0, \qquad C_1^2 = -0.4812317431372$$

$$C_1^3 = -1.049562606709, \qquad C_1^4 = -1.602529574275$$

$$C_1^5 = -1.778267193916, \qquad C_2^1 = 0.097618354692056$$

$$C_2^2 = 0.4122532929155, \qquad C_2^3 = 0.4402169639311$$

$$C_2^4 = 1.426311463224, \qquad C_2^5 = 0.1978760537318$$

The Courant–Friedrichs–Lewy (CFL) number for this scheme is known to be 1.73 for a one-dimensional linear equation.[24] We set the CFL number to one in our calculations.

The Rankine–Hugoniot conditions are applied at the end of each Runge–Kutta stage to update the downstream variables at the shock, after the interior and shock evolution equations have been updated.

Interpolation

We interpolate the u/r contribution to the dilatation when solving the axisymmetric problem using a polynomial fit in the transformed space. Any oscillations that may occur are eliminated with the sixth-order formula

$$\left(\frac{u}{r}\right)_0 = \frac{8}{5}\left(\frac{u}{r}\right)_1 - \frac{4}{5}\left(\frac{u}{r}\right)_2 + \frac{8}{35}\left(\frac{u}{r}\right)_3 - \frac{1}{35}\left(\frac{u}{r}\right)_4 \qquad (30)$$

where the subscript zero corresponds to the axis and the increasing values correspond to successive off-axis points.

Validation

The current code has been checked extensively against analytical solutions and linear theory.[10] In Ref. 10, the authors consider incoming plane vortical waves, which upon interaction with the shock produce plane acoustic, entropy, and vortical waves. The numerical results on this triad of waves are checked against the results of linear theory by comparing the wave amplitudes as a function of the distance from the shock. For wave amplitudes of 0.01% of mean, the computed results agree with linear theory to within 0.1%

when there are 6–10 points per wavelength in the downstream region. This result is confirmed by considering the discretization error of the derivative of $\sin(kx)$, which demonstrates that to obtain a relative error of 0.1% requires approximately 10 uniformly spaced grid points per wavelength. These criteria for resolution are followed in the current study. We provide further evidence on the adequacy of resolution through grid refinement at the end of the subsections on two-dimensional and axisymmetric temperature spot.

Results and Discussion

In all of the simulations presented, the center of the spot is initially at $x_c = 5$, and the mean steady shock is at $x_s = 0$. A convenient nondimensional time unit t^* is

$$t^* = |U_1|t - x_c \tag{31}$$

Therefore, the center of the spot crosses the shock at $t^* = 0$, whereas the front and rear edges of the spot cross the shock at $t^* = \mp 1$.

The initial conditions upstream of the shock for the two-dimensional and axisymmetric configurations are identical in the $x-r$ plane. In the three-dimensional context, the two-dimensional spot represents a heated cylindrical filament with its axis parallel to the shock, whereas the axisymmetric spot represents a spherical heat source or sink. The Euler equations and the shock evolution equation, which together govern the downstream flow, are identical in all respects except for the presence of a v/r term in the definition of $\nabla \cdot \boldsymbol{u}$ in the axisymmetric case. Therefore, all differences in flow properties between two-dimensional and axisymmetric configurations can be ascribed to this term.

To study the budget of enstrophy and mean square dilatation, we examine their evolution equations. The enstrophy satisfies

$$\frac{\partial}{\partial t}\langle\omega^2\rangle = -\langle\omega^2 d\rangle + \left\langle\omega^2 \nabla\cdot\boldsymbol{u}_g\right\rangle + 2\langle(\nabla p \times \nabla\rho^{-1})\cdot\boldsymbol{\omega}\rangle - \langle(\boldsymbol{u}\cdot\boldsymbol{n})\omega^2\rangle_S \tag{32}$$

where $d = \nabla\cdot\boldsymbol{u}$, $\langle\cdot\rangle$ represents integration over the entire computational domain, and the subscript S indicates integration along the mean position of the shock. The successive terms on the right-hand side represent the production of enstrophy due to convective effects, baroclinic torque, shock motion, and the instantaneous shock interaction. There is no generation of enstrophy from vortex stretching in both two-dimensional and axisymmetric configurations due to the absence of a spanwise or azimuthal velocity field.

The mean square dilatation satisfies

$$\frac{\partial}{\partial t}\langle d^2\rangle = \langle d^3\rangle - 2\langle d\nabla\boldsymbol{u} : \nabla\boldsymbol{u}^T\rangle - 2\left\langle\nabla\cdot\left(\frac{\nabla p}{\rho}\right)d\right\rangle + \left\langle d^2\nabla\cdot\boldsymbol{u}_g\right\rangle - \langle(\boldsymbol{u}\cdot\boldsymbol{n})d^2\rangle_S \tag{33}$$

where successive generation terms result from convective effects (first two terms), pressure gradient effects, shock motion, and the instantaneous shock interaction. The last term in Eqs. (32) and (33) represents the effect of shock interaction on the production of $\langle\omega^2\rangle$ and $\langle d^2\rangle$ and is a linear effect to leading order.

To establish the threshold of applicability of linear theory, we study the effect of upstream Mach number M_1 and the amplitude of the entropy spot on the pressure and velocity at the shock retaining terms linear in spot amplitude ϵ. Linearization of Eqs. (13–15) accordingly leads to

$$p' = -\frac{2\gamma M_1^2}{\gamma+1}T_1' + \frac{4\sqrt{\gamma}}{\gamma+1}M_1 u_s \tag{34}$$

$$u' = \frac{2}{\gamma+1}\left(1+\frac{1}{M_1^2}\right)u_s - \frac{2\sqrt{\gamma}}{\gamma+1}\frac{T_1'}{M_1} \tag{35}$$

$$v' = U[(\rho/\rho_1) - 1]x_{s,r} \tag{36}$$

In the early stage of interaction, the shock is solely driven by the temperature disturbance. Therefore, the two terms on the right-hand side of Eq. (34) should be of the same order, which leads to

$$u_s \propto M_1 T_1' = M_1\mathcal{O}(\epsilon) \tag{37}$$

and $p' = M_1^2\mathcal{O}(\epsilon)$. [The Mach number is outside the $\mathcal{O}(\,)$ to emphasize that the relation is expected to hold for all Mach numbers $M_1 \geq 1$.] This scaling is consistent with Eq. (35) for all M_1. Furthermore,

$$u' \approx [2/(\gamma+1)]u_s \tag{38}$$

for large M_1. This heuristic reasoning is borne out by numerical simulation.

We now investigate the structure of the flow for the cases where the amplitude ϵ of the entropy spot varies from 10^{-4} to ± 0.25 and shock strengths (characterized by the upstream Mach number) $M_1 = 2$ and 10. The entropy spot with amplitude $\epsilon = 10^{-4}$ provides the baseline for the measurement of the nonlinear effects. The downstream boundary is located at $x_L = -20$, with the last 10% of the grid points in the buffer domain. Grid parameters are $r_{1/2} = 3.3$ and $r_{\max} = 23$. In all simulations, the grid is 331×64 unless otherwise noted. Simulations at higher resolution and with larger streamwise domains were conducted to ensure that the solution remains unaffected by the outflow condition at the computational boundaries. One such simulation is discussed at the end of the subsection on the two-dimensional temperature spot.

Acoustic waves propagating at velocity $U + c$ reach the buffer domain first at time

$$t_b^* = \frac{|0.9x_L U_1|}{|U| + c} \tag{39}$$

At $M_1 = 2$ and 10, $t_b^* = 17.5$ and 28.7, respectively. Their propagation through the buffer domain is of no physical relevance.

In the next subsection, we discuss the physics of a two-dimensional spot interacting with a shock. The following subsection discusses the axisymmetric spot and emphasizes the differences between the two-dimensional and the axisymmetric configurations.

Two-Dimensional Temperature Spot

We first study the vorticity field downstream of the shock at $t^* = 5$. Two-dimensional contours of vorticity are shown in Figs. 2 and 3 for hot ($\epsilon = 0.25$) and cold ($\epsilon = -0.25$) spots of amplitude $\epsilon = \pm 0.25$ for upstream Mach numbers 2 and 10. (A computational error in the results of AIAA Paper 97-1836[25] was corrected herein. The results only change quantitatively; the conclusions are unaffected.) The vorticity is normalized by ϵM_1. The flowfield is composed of two counter-rotating vortices symmetrical about the x axis.

To explain the structure of the vorticity field downstream of the shock, consider its interaction with a temperature spot of sufficiently small amplitude that nonlinear effects are negligible. For simplicity, we consider the case of large M_1. Then the vorticity immediately behind the shock is obtained from Eqs. (35) and (36) as

$$\omega(0,r,t) = [u'_{,r}(x,r,t) - v'_{,x}]|_{x=0} = \omega_s(r,t) = \frac{2}{\gamma+1}u_{s,r}(r,t) - \frac{2U}{\gamma-1}x_{s,rx}(r,t) \tag{40}$$

At a downstream location (x, y), the vorticity is, therefore,

$$\omega(x,r,t) = \omega_s[r, t - (x/U)] \tag{41}$$

where only leading order terms in M_1 have been retained. The shock velocity is proportional to T_1', whereas the shock displacement is proportional to its time integral. Both terms are proportional to e^{-r^2}; it follows that ω is proportional to re^{-r^2}. Therefore, the vorticity is zero on the axis $r = 0$, and the vorticity field is antisymmetric about this axis. When $u_s \propto T_1'$ and

$$x_s = \int_0^t u_s\,\mathrm{d}t'$$

are substituted into Eq. (41), the vorticity takes the form

$$\omega(x,r,t) \propto T_1'\left(0, r, t - \frac{x}{U}\right) - \frac{2U}{\gamma-1}\frac{\partial^2}{\partial r\,\partial x} \times \int_0^t T_1'\left(0, r, t' - \frac{x}{U}\right)\mathrm{d}t' \tag{42}$$

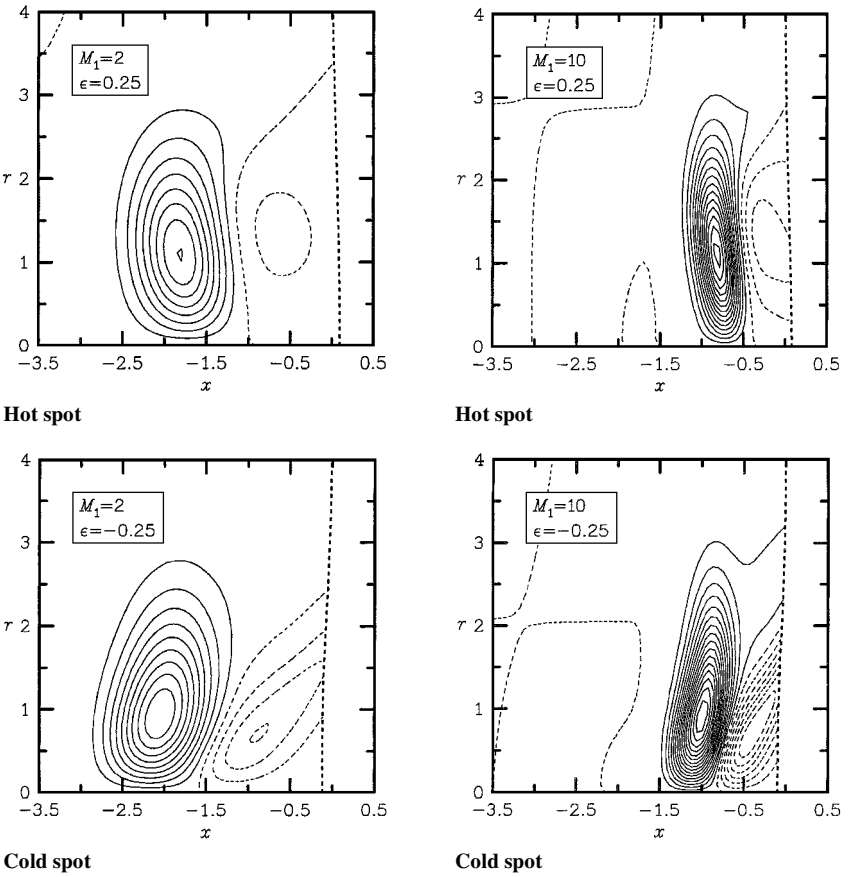

Fig. 2 Two-dimensional contour plots of $\epsilon^{-1}\omega$ at $t^* = 5$: ——, $\epsilon\omega > 0$, and – – –, $\epsilon\omega < 0$; contour separation 0.25.

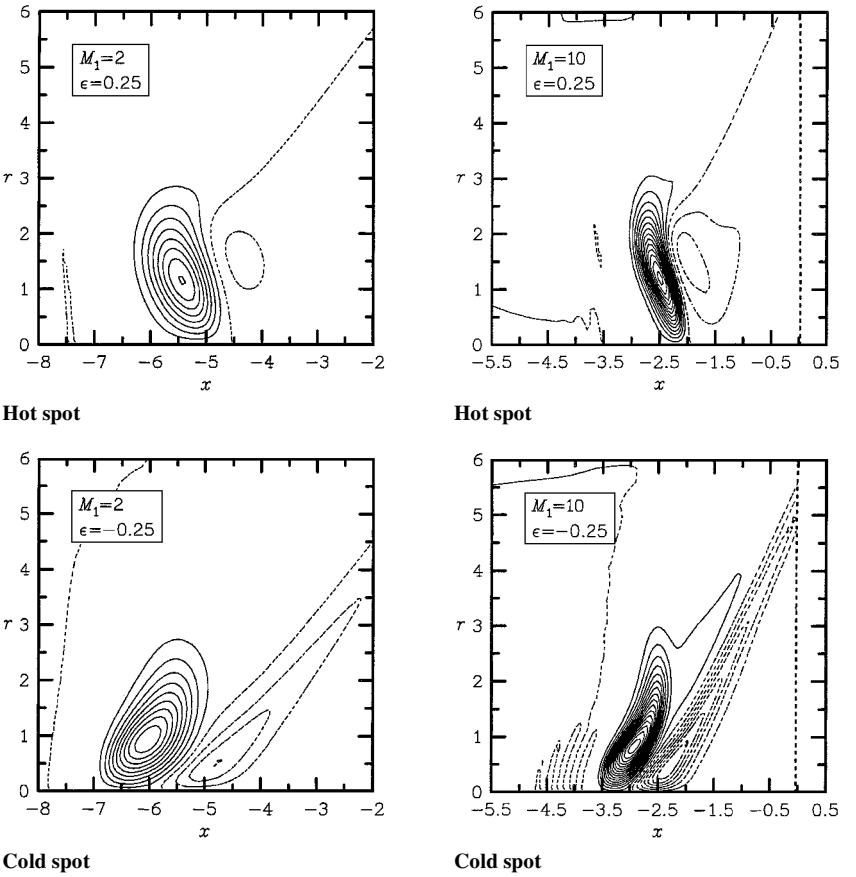

Fig. 3 Two-dimensional contour plots of $\epsilon^{-1}\omega$ at $t^* = 15$: ——, $\epsilon\omega > 0$, and – – –, $\epsilon\omega < 0$; contour separation 0.25.

The partial derivative with respect to x in the second term can be replaced by a derivative with respect to t according to

$$\frac{\partial}{\partial x} \to -\frac{1}{U}\frac{\partial}{\partial t} \tag{43}$$

Substitution of the explicit expression for T_1' into Eq. (42) and making use of Eq. (43) leads to

$$\omega(x, r, t) \propto \epsilon r \exp\left\{-\frac{1}{2}\left[\left(\frac{\rho}{\rho_1}\right)^2\left(x - \frac{x_c}{\rho/\rho_1} - Ut\right)^2 + r^2\right]\right\} \tag{44}$$

Note that the vortex is compressed along the x direction by an amount equal to ρ/ρ_1. A similar, albeit more complex, expression can be derived without imposing the constraint that M_1 be large. The preceding expression for the vorticity represents two counter-rotating vortices symmetrically placed about $r = 0$, which convect downstream at velocity U. Once the downstream entropy spot has moved sufficiently far away from the shock, the shock returns back to its equilibrium state, reversing the sign of u_s. This accounts for the secondary vortices of opposite rotation in Figs. 2 and 3 that lie between the primary vortices and the shock.

It is well known that the vorticity behind the shock is directly proportional to shock curvature[26]:

$$\omega = -[(\rho - \rho_1)/(\rho\rho_1)]\,\boldsymbol{n} \times [\boldsymbol{u}_t \cdot \boldsymbol{K} + \nabla_t(u_s \boldsymbol{x} \cdot \boldsymbol{n})] \tag{45}$$

where $\boldsymbol{K} = \nabla \boldsymbol{n}$ is the curvature tensor of the shock surface and ∇_t is the gradient operator restricted to the shock plane. Equation (45) is exact for both steady and unsteady shocks. The second term in Eq. (45) represents the generation of curvature as a result of adjacent points along a planar shock having different velocities. Because the shock velocity is initially proportional to T_1', it follows that the maximum vorticity generation due to the second term of Eq. (45) is generated at the point where the temperature spot has its maximum gradient, namely, at $r = 1$. As a result, the shock also has a maximum curvature at $r = 1$, and the first term of Eq. (45) takes its maximum value at that point. This is confirmed by the numerical simulation (Figs. 2 and 3).

Figures 2 and 3 show that the base of the vortex is shifted in the downstream or upstream direction according to whether the spot is hot or cold. This is a nonlinear effect which can be explained with the help of Eq. (37). When $\epsilon > 0$, the shock velocity $u_s > 0$ with the result that, near the shock, the downstream velocity field acquires an additional streamwise velocity given by Eq. (38). Therefore, the downstream vortex convects at a velocity $U + u'$. Near the axis, u' is maximum, whereas near the vortex tip ($r = 2$), the shock velocity and, therefore, u' are nearly zero. When the vortex is generated by a cold spot, the region of the vortex near the axis convects downstream faster than the region away from the axis, resulting in vortex tilt. The tilt of the vortex is away from the shock. If one assumes that the velocity differential between vortex base and vortex center remains constant, we expect the tilt to increase with time. Figures 2 and 3 confirm the prediction. Corresponding conclusions hold for the hot spot. Note that the section of the vortex above $r = 2$ convects at the mean velocity U. The amount of tilt between the vortex center and the base of the vortex is estimated by an order of magnitude analysis. From Eqs. (37) and (38), the maximum difference between the downstream velocity at $r = 0$ and 1 at $t^* = 0$ is

$$\Delta u' = [2\sqrt{\gamma}/(\gamma + 1)]\epsilon M_1\left(1 - e^{-\frac{1}{2}}\right) \tag{46}$$

At this time, the center of the spot has just crossed the shock. At $t^* = 1$, the base of the vortex is displaced in the x direction with respect to its center by

$$\Delta x = \Delta u' \frac{1}{|U_1|} \tag{47}$$

$$= [2\epsilon/(\gamma + 1)]\left(1 - e^{-\frac{1}{2}}\right) \tag{48}$$

$$\approx 0.32\epsilon \tag{49}$$

Table 1 Maximum value of vorticity field (normalized by ϵM_1) at $t^* = 5$ for two-dimensional and axisymmetric configurations

		Two dimensional		Axisymmetric	
M_1	ϵ	$(\epsilon M_1)^{-1}\omega_{\max}$	E_ω, %	$(\epsilon M_1)^{-1}\omega_{\max}$	E_ω, %
2	0.25	2.01	(−9.4)	2.11	(−2.8)
2	0.05	2.18	(−1.8)	2.17	(−0.2)
2	10^{-4}	2.22		2.17	
2	−0.05	2.27	(+2.2)	2.20	(+1.1)
2	−0.25	2.48	(+11.7)	2.28	(+4.6)
10	0.25	3.56	(−7.6)	3.81	(0.7)
10	0.05	3.78	(−1.8)	3.78	(−0.08)
10	10^{-4}	3.85		3.78	
10	−0.05	3.92	(+1.8)	3.80	(+0.4)
10	−0.25	4.20	(+9.0)	3.81	(+0.7)

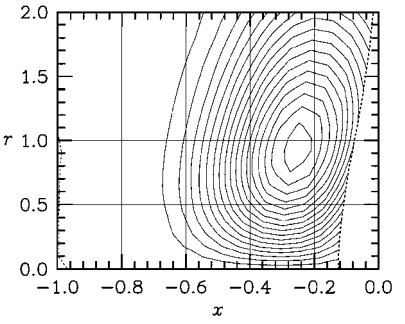

Fig. 4 Contour plot of $\omega/(\epsilon M_1)$ at $t^* = 1$ at $M_1 = 10$; cold spot $\epsilon = -0.25$, maximum 4.4, contour separation 0.25, two-dimensional flow.

which is independent of Mach number. When $\epsilon = 0.25$, the displacement is $\Delta x = 0.08$, which is found to agree with numerical measurement at $t^* = 1$ (Fig. 4). The measured displacement increases to 0.28 at $t^* = 5$ (Fig. 2) and to 0.6 at $t^* = 15$ (Fig. 3). If the velocity difference between the base of the vortex and its center were constant, this displacement at $t^* = 5$ should be 0.4, thereby implying that the velocity difference is actually decreasing.

For $t^* = 5$, the maximum value of vorticity is listed in Table 1 for $M_1 = 2$ and 10 along with E_ω, which is the percentage departure of the maximum normalized vorticity from linear conditions. The vorticity is normalized by ϵM_1. As reported by Zang et al.,[3] a cold spot of amplitude $\epsilon = -0.25$ produces 25% stronger maximum vorticity than a corresponding hot spot. It is obvious from Table 1 that the cold spot increases maximum vorticity compared to the linear case by almost 12%, whereas the hot spot decreases it by about 9.4%, consistent with observation.[3] Figure 5a shows that the vorticity reaches its maximum value around $t^* = 1$, when the rear edge of the spot has crossed the shock. The vorticity then asymptotes to a constant value. Consistent with Table 1, percentage deviations from linear conditions decrease for stronger shocks.

Enstrophy is plotted in Figs. 6a and 6b. As expected, a cold spot increases the enstrophy, whereas a hot spot reduces it, with respect to the levels observed under linear conditions. Note that the departure is stronger for the cold spot. This can be explained simply by considering nonlinear effects. According to Eq. (45), the vorticity produced immediately downstream of the shock scales as the shock velocity, which itself scales as ϵM_1. Higher-order effects can be obtained by replacing M_1 by the instantaneous upstream Mach number M^*. The entropy spot perturbs the temperature as

$$T_1 = (1 + \epsilon T_{10}') \tag{50}$$

and the local sound speed is accordingly perturbed:

$$c^{*2} = c_1^2(1 + \epsilon T_{10}') \tag{51}$$

The velocity remaining unaltered, the Mach number becomes

$$M^{*2} = M_1^2(1 - \epsilon T_{10}') \tag{52}$$

Therefore, the scaled enstrophy relates to the temperature perturbation as

$$\frac{\langle\omega^2\rangle}{\epsilon^2 M_1^2} = \text{const}(1-\epsilon T'_{10})^2 = \text{const}\left(1-2\epsilon T'_{10}+\epsilon^2 T'^2_{10}\right) \quad (53)$$

The first term of Eq. (53) is responsible for the linear behavior and the collapase of the enstrophy profiles as ϵ becomes infinitesimal. The second term is positive or negative according to whether the spot is cold or hot. It is responsible for both the displacement of the enstrophy centerline profiles from linear conditions in opposite directions and for the cold spot producing higher enstrophy. Finally, the third term is always positive. Therefore, the enstrophy of both cold and hot spots is enhanced. This term is responsible for the asymmetry in the displacement of the profiles from linear conditions.

We discussed why nonlinear effects are stronger for a cold spot than a hot spot. Because the mean square dilatation is also proportional to the perturbation velocity, the arguments leading to Eq. (53) also explain why a cold spot produces stronger normalized mean square dilatation than the linear case (Figs. 6c and 6d), whereas the hot spot produces lower mean square dilatation. Dilatation at $M_1 = 10$ begins to grow around $t^* = 2$, which reflects that the acoustic wave front is steepening.

We next consider the structure of the acoustic field (measured by downstream pressure perturbation p'). The acoustic field at $M_1 = 2$ and 10 measured at $t^* = 15$ is shown in Fig. 7. At the higher Mach number, the acoustic front steepens, but has not yet formed a shock by $t^* = 31$. The shock formation process is clarified in Figs. 8 and 9, which shows a series of centerline profiles for p' and $\mathrm{d}p'/\mathrm{d}x$ at fixed time intervals of for $M_1 = 2$ and $M_2 = 10$. The decay of the maximum pressure derivative at $M_1 = 2$ (Fig. 8b) indicates an absence of shock formation; however, at $M_1 = 10$, the fronts clearly steepen (Fig. 9b) with the resulting formation of a shock. The oscillations present in Fig. 9 are indicative of a pressure discontinuity along the centerline.

Figure 10 summarizes the investigation of the individual terms in Eqs. (32) and (33). The simulation results reveal that the dominant term in the budget of enstrophy is due to the instantaneous shock interaction. This term is found to be one order of magnitude higher than those due to convective and baroclinic effects. These findings are valid for both low and high Mach numbers. On the other hand, we find that the generation of mean square dilatation is dominated by the pressure gradient term and the instantaneous shock interaction term whose magnitudes are of the same order.

To demonstrate the accuracy of the results, we conduct on two different grids simulations of a cold spot with $\epsilon = -0.25$ at $M_1 = 10$, which is the hardest case to resolve numerically due to wave steepening along the acoustic front. The coarse mesh corresponds to the one used in the earlier results; it has a resolution of 331×64 points in a downstream domain of dimensions $[-20, 0] \times [0, 23]$. The fine grid has a resolution of (881×128) in the region $[-30, 0] \times [0, 40]$. Besides covering a larger area, the fine grid has almost twice the resolution of the coarse grid per unit length. Centerline plots from both simulations are indistinguishable to the eye. Relative to the finer-resolution case, the relative error at the extremal values of p' is less than 2×10^{-3}.

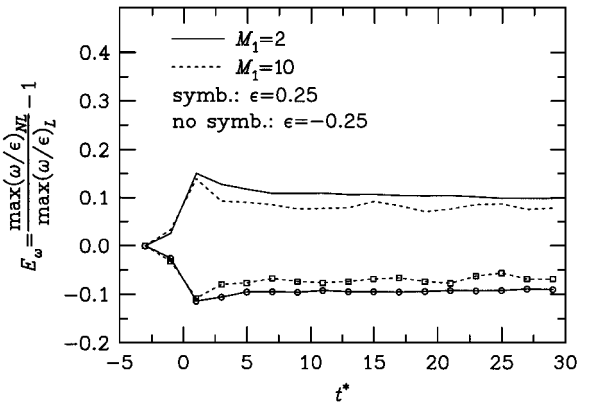

a) Two-dimensional flow

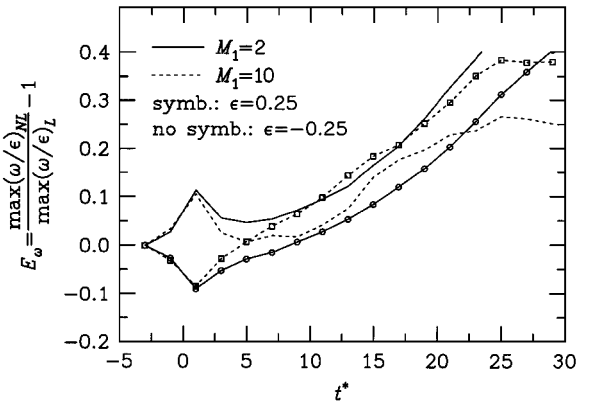

b) Axisymmetric flow

Fig. 5 Time history of E_ω at $M_1 = 2$ and 10.

Axisymmetric Temperature Spot

The equations that govern the dynamics of the axisymmetric spot interacting with a shock are identical in all aspects to those for the

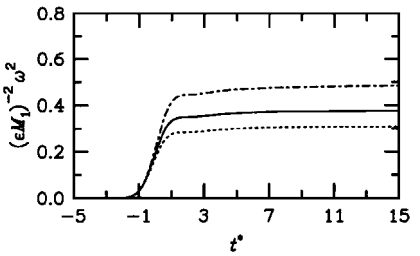

a) $(\epsilon M_1)^{-2}\langle\omega^2\rangle$ and $M_1 = 2$

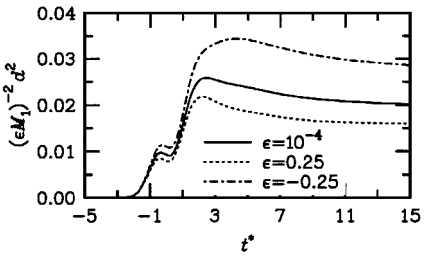

c) $(\epsilon M_1)^{-2}\langle d^2\rangle$ and $M_1 = 2$

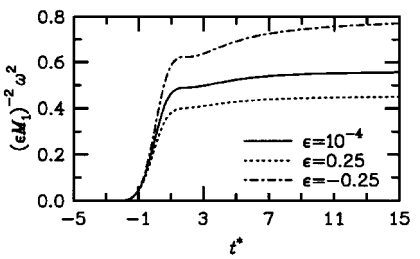

b) $(\epsilon M_1)^{-2}\langle\omega^2\rangle$ and $M_1 = 10$

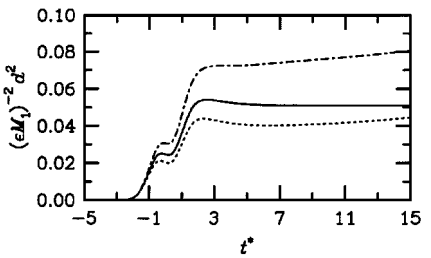

d) $(\epsilon M_1)^{-2}\langle d^2\rangle$ and $M_1 = 10$

Fig. 6 Two-dimensional flow time history.

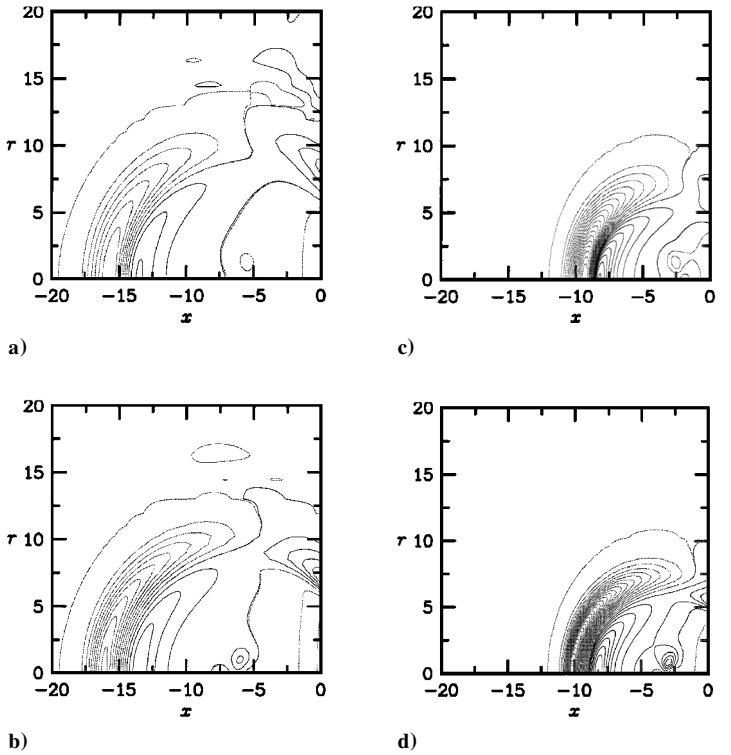

Fig. 7 Two-dimensional flow contour plots of $(\epsilon M_1^2)^{-1}p'$ at $t^* = 15$: a) $M_1 = 2$, contour increments 0.01, hot spot $\epsilon = 0.25$; b) $M_1 = 2$, contour increments 0.01, cold spot $\epsilon = -0.25$; c) $M_1 = 10$, contour increments 0.02, hot spot $\epsilon = 0.25$; and d) $M_1 = 10$, contour increments 0.02, cold spot $\epsilon = -0.25$.

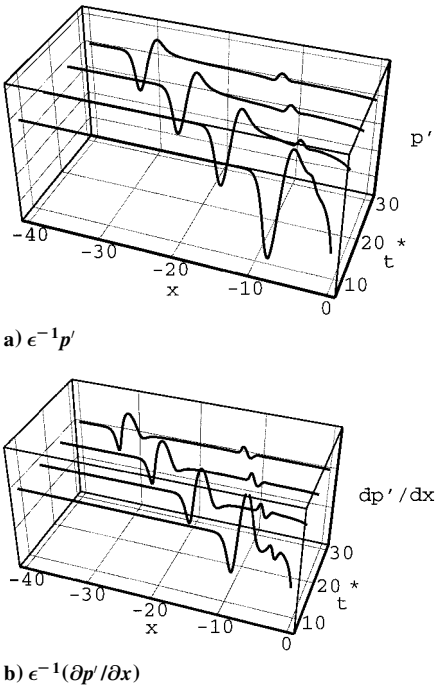

Fig. 8 Two-dimensional flow centerline profiles from $t^* = 7$ to $t^* = 31$ ($M_1 = 2$) by increments of $\Delta t^* = 8$ for $\epsilon = -0.25$.

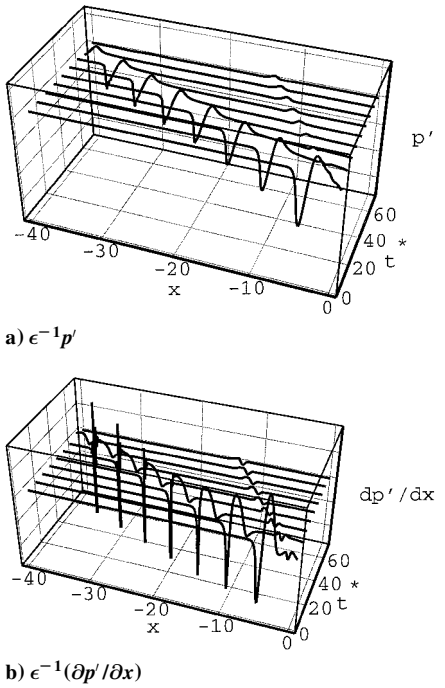

Fig. 9 Two-dimensional flow center profiles at $t^* = 7$ to $t^* = 71$ ($M_1 = 10$) by increments of $\Delta t^* = 8$ for $\epsilon = -0.25$.

two-dimensional spot except for the presence of an extra term v/r in the definition of the dilatation. Although this term appears only in the equation of continuity (expressed in terms of the logarithm of pressure), its effect on the flow structure is not easily discernible. Therefore, we describe the effects of axisymmetry in comparison with the two-dimensional results. The interaction of an axisymmetric spot with a shock produces a vortex ring, which can be viewed as the counter-rotating vortices rotated about the axis $r = 0$.

Table 1 lists the maximum values of vorticity (normalized by ϵM_1) at $t^* = 5$, along with percentage deviations from the maximum vorticity when $\epsilon = 10^{-4}$. These values are contrasted with the corresponding two-dimensional values. Most evident is that departures from linear conditions are greatly reduced in the axisymmetric case. Furthermore, these departures are not symmetric about the linear baseline, even when the spot amplitude is 0.05. Two-dimensional spots on the other hand produce a vorticity field whose maximum is equally displaced from the linear value. To understand better the data in Table 1, time histories of the percentage departure of maximum normalized vorticity from linear conditions (denoted by E_ω) are shown in Fig. 5b at both $M_1 = 2$ and 10. As the spot crosses

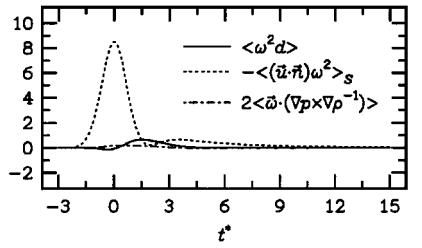

a) $\langle \omega^2 \rangle$ and $M_1 = 2$

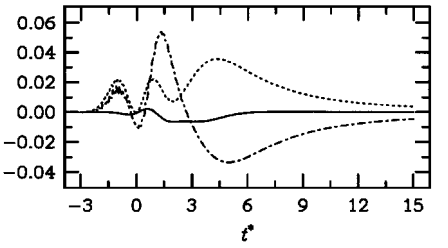

c) $\langle d^2 \rangle$ and $M_1 = 2$ (see legend in part d)

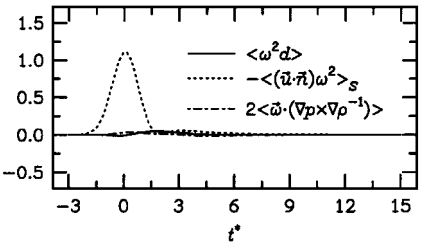

b) $\langle \omega^2 \rangle$ and $M_1 = 10$

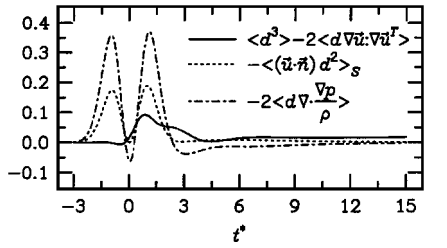

d) $\langle d^2 \rangle$ and $M_1 = 10$

Fig. 10 Two-dimensional flow, $\epsilon = -0.25$ (cold spot), time history of dominant terms in the transport equations for $\langle \omega^2 \rangle$ and $\langle d^2 \rangle$.

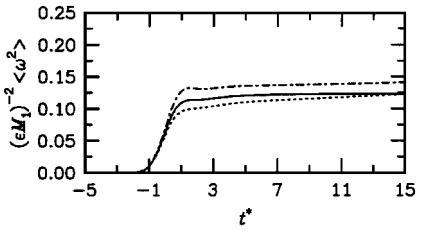

a) $(\epsilon M_1)^{-2} \langle \omega^2 \rangle$ and $M_1 = 2$

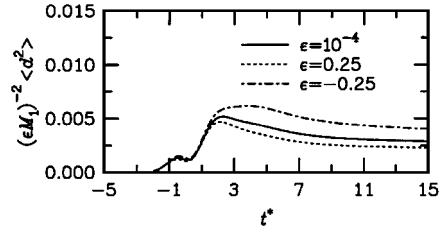

c) $(\epsilon M_1)^{-2} \langle d^2 \rangle$ and $M_1 = 2$

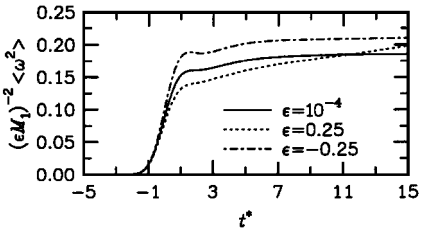

b) $(\epsilon M_1)^{-2} \langle \omega^2 \rangle$ and $M_1 = 10$

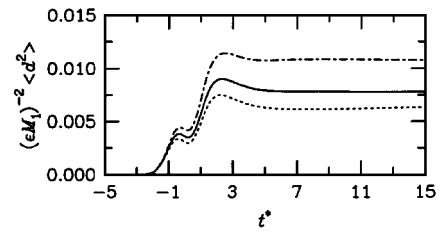

d) $(\epsilon M_1)^{-2} \langle d^2 \rangle$ and $M_1 = 10$

Fig. 11 Axisymmetric flow time history.

the shock ($t^* < 1$), E_ω increases with little qualitative difference between two-dimensional and axisymmetric configurations except for a slower increase in the axisymmetric case. However, for $t^* > 1$, it remains approximately constant for the two-dimensional spot, while it increases for both hot and cold axisymmetric spots. Eventually, E_ω for the axisymmetric spot overtakes E_ω for the cold two-dimensional spot. The continued increase of E_ω is possibly due to the presence of an extra term $\omega v/r$ in the vorticity equation for the axisymmetric case.

Of interest is that at the higher Mach number, an axisymmetric hot spot produces a higher maximum vorticity than the cold spot past $t^* = 10$. Nonetheless, the enstrophy generated by the hot spot remains lower than that produced under linear conditions, whereas a cold spot produces more enstrophy than the linear case. Percentage differences with respect to the linear conditions are smaller than for the two-dimensional case (compare Figs. 6 and 11). The time history of mean square dilatation at $M_1 = 2$ and 10 is shown in Figs. 11c and 11d.

Figure 12 plots centerline profiles of $(1/\epsilon)(\partial p'/\partial x)$ for $\epsilon = -0.25$. Contrasting Fig. 12 with the two-dimensional results in Figs. 8 and 9, we observe that steepening of the acoustic wave for the axisymmetric cold spot is absent. However, the acoustic wave steepens for the axisymmetric hot spot with a simultaneous decay of the wave amplitude. Figure 13 shows centerline profiles of $\epsilon^{-1} p'$ and $\epsilon^{-1}(\partial p'/\partial x)$ for axisymmetric flow.

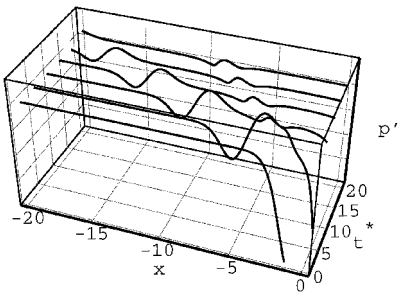

$\epsilon^{-1} p'$

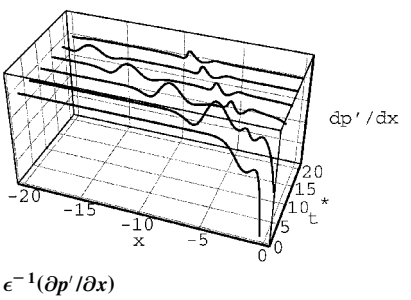

$\epsilon^{-1}(\partial p'/\partial x)$

Fig. 12 Axisymmetric flow centerline profiles from $t^* = 1$ to $t^* = 21$ ($M_1 = 2$) by increments of $\Delta t^* = 4$ for $\epsilon = -0.25$.

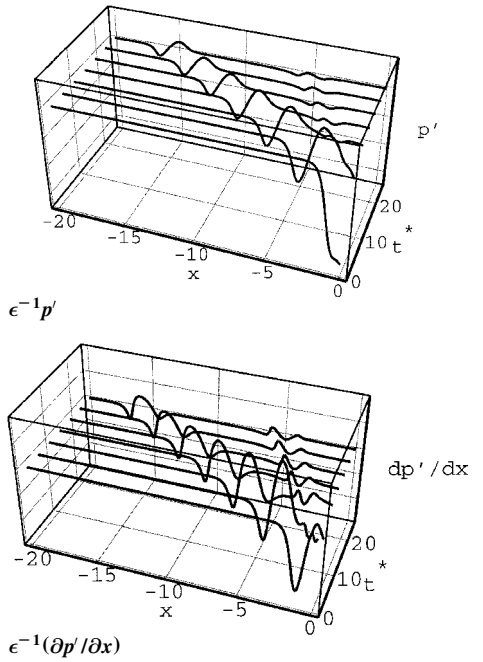

Fig. 13 Axisymmetric flow centerline profiles from $t^* = 1$ to $t^* = 25$ ($M_1 = 10$) by increments of $\Delta t^* = 4$ for $\epsilon = -0.25$.

Another distinction between two-dimensional and axisymmetric configurations is shown in Fig. 14, where the shock velocity and shock profiles at $t^* = 21$ and $\epsilon = -0.25$ for both $M_1 = 2$ and 10. In both cases, the shock velocity profile has a wavelike structure propagating toward the freestream. The shock velocity associated with a two-dimensional spot (Fig. 14a) has a slightly negative velocity ($\epsilon^{-1}u_s$) at the centerline, which increases monotonically to a maximum and then decreases to zero. In the axisymmetric case (Fig. 14b), the scaled shock velocity is also negative at the centerline, but it decreases initially as r increases, reaches a minimum, then increases toward the positive peak of the pulse. Again, this pulse propagates toward the freestream. This difference in structure between two-dimensional and axisymmetric configurations is reflected in the shape of the shock. In two-dimensional configurations (Fig. 14c), the shock has the shape of a smoothed top hat, whose width increases and whose height decreases, in time. The negative velocity region for the axisymmetric shock generates a local maximum in the shock profile (Fig. 14d). Note, finally, that the amplitude of x_s and u_s is an order of magnitude smaller in the axisymmetric case, although they are of the same order until the vortex completes its interaction with the shock ($t^* = 1$). In Fig. 15, the scaled shock velocity profile is shown for both Mach numbers at $\epsilon = \pm 0.25$ and $\epsilon = 10^{-4}$. As expected, the wave front is steeper for the cold spot, particularly so at the higher Mach number, but a discontinuity does not appear to be forming along the shock. In all cases, the wave propagates at a faster rate when the spot is hot, which is consistent with an increase in the speed of the upstream sound given by Eq. (51).

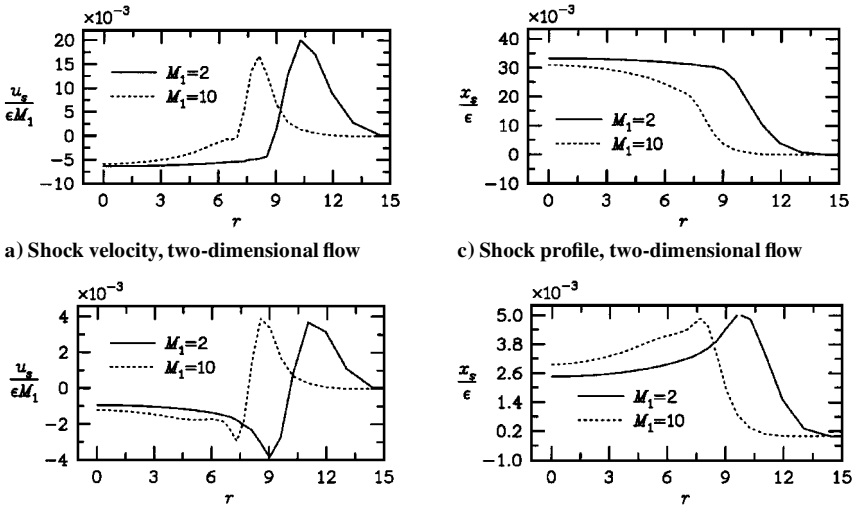

a) Shock velocity, two-dimensional flow

c) Shock profile, two-dimensional flow

b) Shock velocity, axisymmetric flow

d) Shock profile, axisymmetric flow

Fig. 14 Flows at $M_1 = 2$ and 10, $t^* = 21$, for $\epsilon = -0.25$ (cold spot).

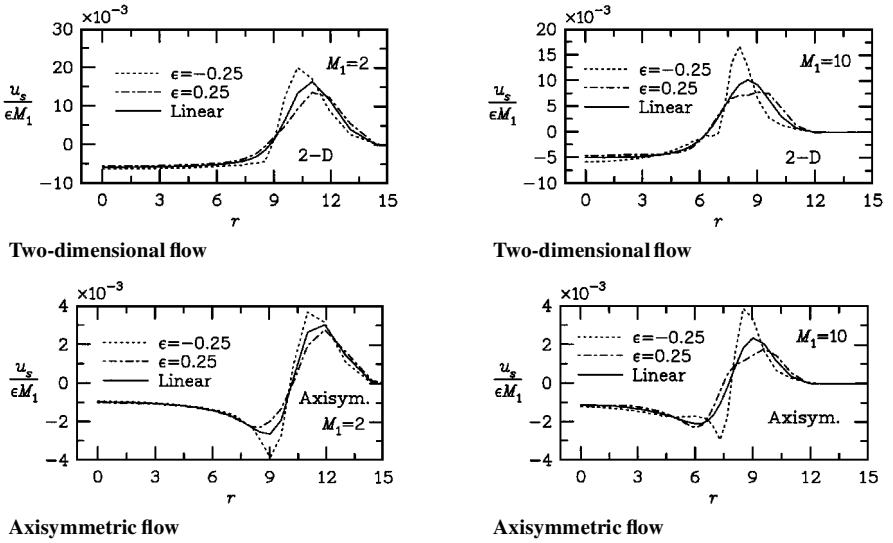

Two-dimensional flow

Two-dimensional flow

Axisymmetric flow

Axisymmetric flow

Fig. 15 Shock velocity for spot amplitudes $\epsilon = \pm 0.25$ and 10^{-4}, $t^* = 21$.

We have conducted a simulation with $\epsilon = -0.25$ and $M_1 = 10$ at the fine resolution of 881×128 on the domain $[-30, 0] \times [0, 40]$. The relative error of p' at its extremal values along the centerline is less than 3×10^{-3}.

Conclusion

A series of numerical experiments were carried out to study the interaction of a localized temperature disturbance with a shock. The maximum amplitude of the temperature disturbance was 25% of its mean value. The shock Mach numbers were 2 and 10.

Two-dimensional spots generate a pair of cylindrical vortices, whereas axisymmetric spots generate a vortex ring. The amount of vorticity generated scales with the product of the shock Mach number and the temperature spot amplitude. Two-dimensional cold spots generate stronger maximum vorticity than hot spots. Whereas the maximum vorticity asymptotes to a constant value in the two-dimensional case, it continuously increases in the axisymmetric case. Surprisingly, the axisymmetric hot spot generates stronger vorticity than the cold spot at high Mach numbers. However, the mean square vorticity (enstrophy) generated is always greater for the cold spot.

At the higher Mach number, the acoustic wave generated by the shock interaction decreases in amplitude and steepens as it propagates downstream, eventually forming a shock. The two-dimensional acoustic waves have a greater tendency to form a shock, particularly in the case of a cold spot. On the other hand, the axisymmetric acoustic wave decreases in amplitude and does not steepen.

References

[1]Salas, M. D., Zang, T. A., and Hussaini, M. Y., "Shock-Fitted Euler Solutions to Shock–Vortex Interactions," *Proceedings of the 8th International Conference on Numerical Methods in Fluid Dynamics*, edited by E. Krause, Vol. 170, Lecture Notes in Physics, Springer–Verlag, New York, 1982, pp. 461–467.

[2]Zang, T. A., Kopriva, D. A., and Hussaini, M. Y., "Pseudospectral Calculations of Shock–Turbulence Interactions," *Numerical Methods in Laminar and Turbulent Flow*, edited by C. Taylor, J. A. Johnson, and W. R. Smith, Pineridge, Swansea, Wales, UK, 1983, pp. 210–220.

[3]Zang, T. A., Hussaini, M. Y., and Bushnell, D. M., "Numerical Computations of Turbulence Amplification in Shock-Wave Interactions," *AIAA Journal*, Vol. 22, No. 1, 1984, pp. 13–21.

[4]Hussaini, M. Y., Collier, F., and Bushnell, D. M., "Turbulence Alteration due to Shock Motion," *Turbulent Shear Layer/Shock Wave Interactions*, edited by J. Délery, International Union of Theoretical and Applied Mechanics Symposium (Palaiseau/France), Springer–Verlag, New York, 1985, pp. 371–381.

[5]Jackson, T. L., Hussaini, M. Y., and Ribner, H. S., "Interaction of Turbulence with a Detonation Wave," *Physics of Fluids A*, Vol. 5, No. 3, 1993, pp. 745–749.

[6]Lasseigne, D. G., Jackson, T. L., and Hussaini, M. Y., "Nonlinear Interaction of a Detonation/Vorticity Wave," *Physics of Fluids A*, Vol. 3, No. 8, 1991, pp. 1972–1979.

[7]Meadows, K. R., Kumar, A., and Hussaini, M. Y., "Computational Study on the Interaction Between a Vortex and a Shock Wave," *AIAA Journal*, Vol. 29, No. 2, 1991, pp. 174–179.

[8]Duck, P. W., Lasseigne, D. G., and Hussaini, M. Y., "On the Interaction Between the Shock Wave Attached to a Wedge and Freestream Disturbances," *Theoretical Computational Fluid Dynamics*, Vol. 7, No. 2, 1995, pp. 119–139.

[9]Duck, P. W., Lasseigne, D. G., and Hussaini, M. Y., "The Effect of Three-Dimensional Freestream Disturbances on the Supersonic Flow Past a Wedge," *Physics of Fluids*, Vol. 9, No. 2, 1997, pp. 456–467.

[10]Erlebacher, G., Hussaini, M. Y., and Jackson, T. L., "Nonlinear Strong Shock–Vortex Interactions: A Shock-Fitted Approach," *Theoretical Computational Fluid Dynamics*, Vol. 11, No. 1, 1998, pp. 1–29.

[11]Hussaini, M. Y., and Erlebacher, G., "Numerical Simulations of Shock–Entropy Spot Interactions," *Proceedings of the Fifteenth International Conference on Numerical Methods in Fluid Dynamics*, edited by P. Kutler, J. Flores, and J.-J. Chattot, Lecture Notes in Physics, Vol. 490, Springer–Verlag, New York, 1997, pp. 572–577.

[12]Mahesh, K., Lele, S. K., and Moin, P., "The Influence of Entropy Fluctuations on the Interaction of Turbulence with a Shock Wave," *Journal of Fluid Mechanics*, Vol. 334, March 1997, pp. 353–379.

[13]Chang, C. T., "Interaction of a Plane Shock and Oblique Plane Disturbances with Special Reference to Entropy Waves," *Journal of the Aeronautical Sciences*, Vol. 24, 1957, pp. 675–682.

[14]Cuadra, E., "Flow Perturbations Generated by a Shock Wave Interacting with an Entropy Wave," *Proceedings of the AFOSR-UTIA Symposium on Aerodynamic Noise*, Univ. of Toronto Press, Toronto, ON, Canada, 1968, pp. 251–271.

[15]McKenzie, J. F., and Westphal, K. O., "Interaction of Linear Waves with Oblique Shock Waves," *Physics of Fluids*, Vol. 11, No. 11, 1968, pp. 2350–2362.

[16]Moore, F. K., "Unsteady Oblique Interaction of a Shock Wave with a Plane Disturbance," NACA Rept. 1165, 1954.

[17]Ribner, H. S., "Convection of a Pattern of Vorticity Through a Shock Wave," NASA Rept. 1164, 1954.

[18]Kumar, A., Bushnell, D. M., and Hussaini, M. Y., "Mixing Augmentation Technique for Hypervelocity Scramjets," *Journal of Propulsion and Power*, Vol. 5, No. 5, 1989, pp. 514–522.

[19]Canuto, C., Hussaini, M. Y., Quarteroni, A., and Zang, T. A., *Spectral Methods in Fluid Dynamics*, Springer–Verlag, Berlin, 1987.

[20]Hussaini, M. Y., Kopriva, D. A., Salas, M. D., and Zang, T. A., "Spectral Methods for the Euler Equations II: Chebyshev Methods and Shock-Fitting," *AIAA Journal*, Vol. 23, No. 2, 1985, pp. 234–240.

[21]Kopriva, D. A., Zang, T. A., and Hussaini, M. Y., "Spectral Methods for the Euler Equations: The Blunt Body Problem Revisited," *AIAA Journal*, Vol. 29, No. 9, 1991, pp. 1458–1462.

[22]Ta'asan, S., and Nark, D., "An Absorbing Buffer Zone Technique for Acoustic Wave Propagation," AIAA Paper 95-0164, 1995.

[23]Carpenter, M. H., Gottlieb, D., and Abarbanel, S., "The Stability of Numerical Boundary Treatments for Compact High-Order Finite-Difference Schemes," *Journal of Computational Physics*, Vol. 108, No. 2, 1993, pp. 272–295.

[24]Carpenter, M. H., and Kennedy, C. A., "Fourth-Order 2N-Storage Runge–Kutta Schemes," NASA TM-109112, 1994.

[25]Hussaini, M. Y., and Erlebacher, G., "Interaction of 2-D and Axisymmetric Entropy Spots with a Shock," AIAA Paper 97-1836, June 1997.

[26]Hayes, W. D., "The Vorticity Jump Across a Gasdynamic Discontinuity," *Journal of Fluid Mechanics*, Vol. 2, 1957, pp. 595–600.

K. Kailasanath
Associate Editor